Check for updates

JGR Oceans

RESEARCH ARTICLE
10.1029/2020JC016554

Southward Internal Tides in the Northeastern South China Sea

Zhongxiang Zhao[1]

[1]Applied Physics Laboratory, University of Washington, Seattle, WA, USA

Key Points:
- The continental slope at the entrance to the Taiwan Strait radiates southward M_2 and S_2 internal tides, but not O1 and K1 internal tides
- The 26-year-coherent southward M2 energy flux is 0.18 GW, about 10% of the westward energy flux from the Luzon Strait
- The complicated multiwave internal tide field leads to significant spatial variability of internal tidal energy flux

Correspondence to:
Z. Zhao,
zzhao@apl.uw.edu

Citation:
Zhao, Z. (2020). Southward internal tides in the northeastern South China Sea. *Journal of Geophysical Research: Oceans*, *125*, e2020JC016554. https://doi.org/10.1029/2020JC016554

Received 29 JUN 2020
Accepted 15 OCT 2020
Accepted article online 29 OCT 2020

Abstract The M_2 internal tides in the northeastern South China Sea are studied using satellite altimeter data from 1992–2018. By an improved mapping technique that combines plane wave analysis and two-dimensional spatial filtering, multiple internal tides are separately extracted with weak internal tides becoming detectable. The satellite results reveal for the first time a 300-km-long southward M_2 internal tidal beam in the northeastern South China Sea. The generation source is on the steep continental slope at the southern entrance to the Taiwan Strait. It ranges from 118–120°E along 22°N. Combining satellite-observed internal solitary waves and internal tides, it is found that the onshore radiation evolves into nonlinear solitary waves and the offshore radiation in the form of linear internal tides. Based on the 26-year-coherent satellite results, the integrated southward energy flux is 0.18 GW, about 10% of the westward energy flux from the Luzon Strait. In the northeastern South China Sea, the westward and southward internal tides form a multiwave interference field, which features significant spatial variations in the magnitude and direction of energy flux. Further analyses reveal that the steep continental slope radiates southward semidiurnal M_2 and S_2 internal tides, but not diurnal K_1 and O_1 internal tides.

Plain Language Summary Internal tides are internal waves of tidal frequency occur in the interior of the stratified ocean. They mainly originate from topographic scattering of the barotropic tidal motion. Our knowledge of internal tides is mainly limited by the lack of field measurements with sufficient temporal and vertical resolution. Satellite altimetry offers a unique technique that observes internal tides from the space via their centimeter-scale sea surface fluctuations. Mapping techniques have been developed to extract internal tides from satellite altimeter data. This paper applies a newly developed mapping technique to the northeastern South China Sea and obtains an internal tide field with unprecedented details. Multidirectional internal tides from different generation sites are separately resolved. The satellite observations shed new light on barotropic-to-baroclinic conversion, internal solitary waves, multiwave interference, and internal tide energetics in the South China Sea. This paper confirms the uniqueness of satellite altimetry and the usefulness of the new mapping technique in advancing our knowledge of internal tides. This mapping technique can be applied to observe multiple internal tides in other marginal seas.

1. Motivation

A piece is still missing in the big picture of the internal tide field in the northeastern South China Sea (SCS). Previous studies mainly focus on internal tides generated in the Luzon Strait; however, internal tides from surrounding continental slope have not been reported in the literature. Here the big picture will be improved by including southward internal tides from the continental slope at the southern entrance to the Taiwan Strait. The northeastern SCS connects to the western Pacific Ocean via two main waterways: the Luzon Strait and the Taiwan Strait (Figure 1a). The >3,000-m-deep Luzon Strait lies between the Taiwan and Luzon islands, whose topographic extensions form two parallel meridional submarine ridges across the strait. To the north, the much shallower Taiwan Strait situates on the wide continental shelf, separating the Taiwan Island from the main continent. The Luzon Strait has long been known for its powerful internal tide radiation, due to the combination of strong barotroptic tidal currents and steep submarine ridges (Niwa & Hibiya, 2004; Zhao, 2014). In the past two decades, the barotropic-to-baroclinic tidal conversion in the Luzon Strait has been simulated using various numerical models (Buijsman et al., 2010; Jan et al., 2008; Kerry et al., 2013; Lai et al., 2019; Niwa & Hibiya, 2004; Simmons et al., 2011; Vlasenko et al., 2010; Wang et al., 2016; Xu et al., 2016; Zhang et al., 2011). The Luzon Strait radiates internal tides both westward

©2020. American Geophysical Union. All Rights Reserved.

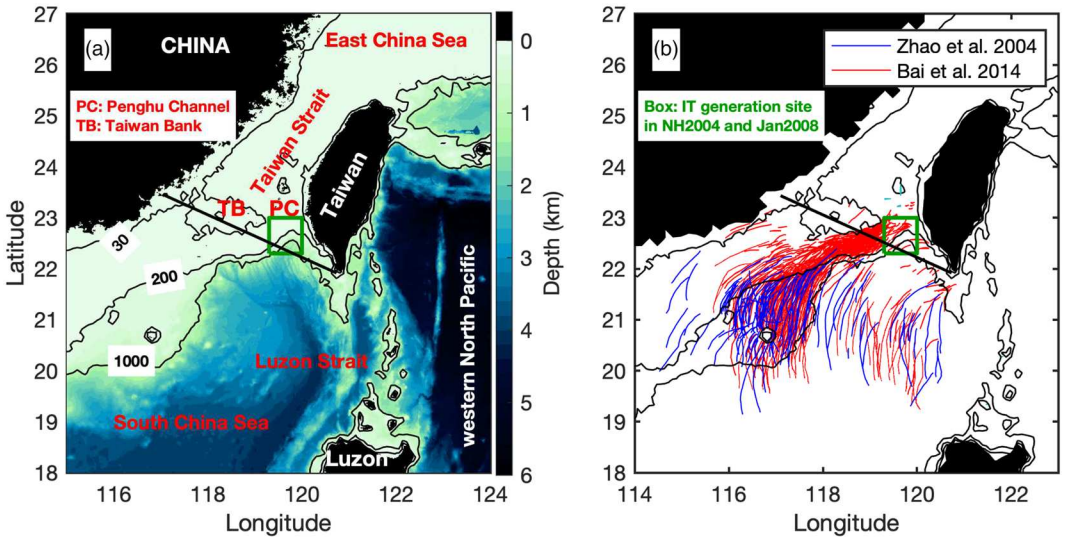

Figure 1. The northeastern South China Sea. (a) Bottom topography. (b) Internal solitary waves (ISWs). Blue lines indicate ISWs observed in a variety of satellite images by Zhao et al. (2004). Red lines indicate ISWs observed in MODIS images by Bai et al. (2014). Green boxes indicate one hot spot of barotropic to baroclinic tidal conversion in numerical models of Niwa and Hibiya (2004) and Jan et al. (2008). Black lines indicate isobathic contours of 30, 200, and 1,000 m as labeled in (a). The boundary between the South China Sea and the Taiwan Strait is indicated by a line linking Nan'ao Island, Guangdong (117°6′E, 23°26′N) and Cape Maobitou, Taiwan (120°44′E, 21°55′N).

into the SCS and eastward into the western Pacific Ocean. The outgoing internal tides have been observed by satellite altimetry via sea surface height fluctuations (Ray & Zaron, 2011; Zhao, 2014). Satellite observations reveal that internal tides propagate thousands of km in both directions (Zhao, 2014). In particular, the northwestward internal tides steepen and generate large-amplitude internal solitary waves (ISWs), which have been reported even longer time ago (Fett & Rabe, 1977; Liu et al., 1998) and widely observed in satellite images (Figure 1b) (Bai et al., 2014; Jackson, 2009; Wang et al., 2012; Zhao et al., 2004; Zheng et al., 2007).

Internal tide generation and southward energy flux in the southern Taiwan Strait have been revealed in previous numerical studies. However, there is no direct observation of the southward internal tides in the northeastern SCS. Several numerical models show barotropic to baroclinic tidal conversion in the southern Taiwan Strait. For example, Niwa and Hibiya (2004) simulate M_2 internal tides in the western Pacific using the Princeton Ocean Model (POM). Their results show internal tide generation in a number of places, including the southern Taiwan Strait (their Figure 12). Jan et al. (2008) simulate internal tides in the Luzon Strait using the regional ocean modeling system (ROMS). Their simulations also reveal internal tide generation in the southern Taiwan Strait (their Figure 8). However, these researchers do not pay much attention to the southward internal tides from the Taiwan Strait, because their main goal at that time is the dominant internal tides from the Luzon Strait. Recently, more and more numerical modeling studies confirm internal tide generation and southward energy flux in the southern Taiwan Strait (Chiou et al., 2011; Xu et al., 2016). Furthermore, ISWs have been observed on the continental shelf in the southern Taiwan Strait. Bai et al. (2014) observe hundreds of ISWs in satellite Moderate Resolution Imaging Spectroradiometer (MODIS) images from 2000–2011 on the continental shelf to the south of Taiwan Bank (Figure 1, red lines). They suggest that some of the ISWs are locally generated on the continental slope. All these studies suggest the internal tide generation and outgoing radiation in the southern Taiwan Strait. Yet, it is unclear how wide the internal tidal beam spreads and how far it propagates in the northeastern SCS. This paper reveals a 300-km-long southward M_2 internal tidal beam. The results improve the big picture of the internal tide field in the northeastern SCS by including internal tides from multiple generation sites.

The much weaker southward internal tides are difficult to detect, particularly due to the presence of strong internal tides from the Luzon Strait (Niwa & Hibiya, 2004; Zhao, 2014). Mooring measurements at sparse stations lack spatial information and cannot resolve internal tides in different propagation directions. Fortunately, satellite altimetry observes internal tides from the space and provides a two-dimensional view of the internal tide field. For example, satellite altimetry can resolve the westward and eastward internal

21699291, 2020, 11, Downloaded from https://agupubs.onlinelibrary.wiley.com/doi/10.1029/2020JC016554 by University Of Washington, Wiley Online Library on [15/09/2025]. See the Terms and Conditions (https://onlinelibrary.wiley.com/terms-and-conditions) on Wiley Online Library for rules of use; OA articles are governed by the applicable Creative Commons License

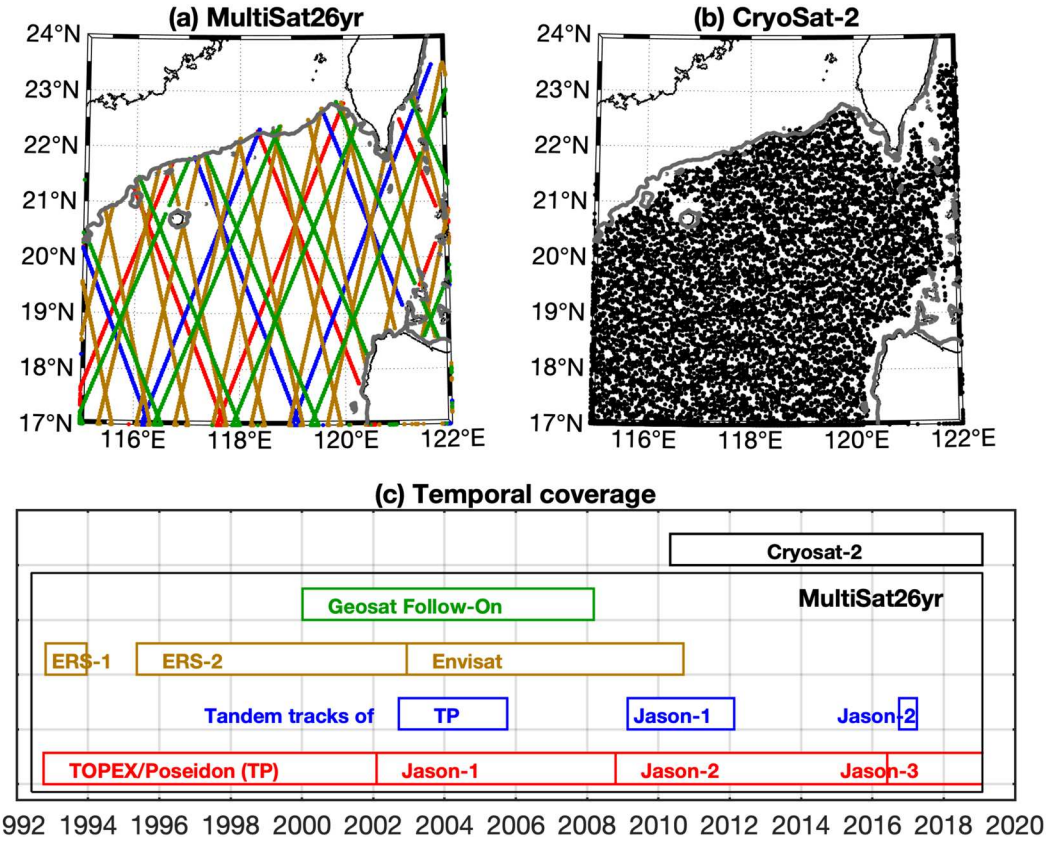

Figure 2. Satellite altimeter data. (a) Ground tracks of MultiSat26yr. Colors are coded as in (c). (b) Data points of the long-repeat-track mission CryoSat-2. For clarity, the data points are plotted every tenth. The 200-m isobathic contours are shown as gray lines. (c) Time coverage of satellite altimeter missions from 1992 to 2020.

tides from the Luzon Strait (Zhao, 2014). The present paper shows southward internal tides from the continental slope to the south of the Taiwan Strait by a new mapping technique. The technique combines plane wave analysis and two-dimensional (2-D) band-pass filtering (Zhao, 2019): The former can resolve waves of different propagation directions; the latter can significantly suppress nontidal noise. The technique makes it possible to extract the much weaker internal tides previously neglected.

The new internal tide field shows that, in the northeastern SCS, there exist southward internal tides from the surrounding continental slope, as well as westward internal tides from the Luzon Strait. The results are useful in the budget of internal tide energy and ocean mixing, which is one active research topic in this region (Alford et al., 2015; Wang et al., 2016; Xu et al., 2016). The results show that the internal tide field is a superposition of multiple waves, making it a challenge to study the temporal and spatial variations of internal tides (Huang et al., 2018; Park & Farmer, 2013; Zhai et al., 2020). This paper suggests that a proper way to study the internal tide variability is using multidirectionally decomposed internal tides from different generation sources. The rest of this paper is arranged as follows. Section 2 briefly describes the satellite data, the mapping technique, and the resultant internal tide field. Section 3 evaluate the resultant internal tide field by independent measurements. Section 4 discusses the southward M_2 internal tides from the continental slope. Section 5 discusses the distorted energy flux in a two-wave interference field. Section 6 discusses other major tidal constituents. Section 7 is a summary.

2. Data, Methods, and Results

2.1. Satellite Altimeter Data

Along-track sea surface height (SSH) measurements from exact-repeat-track satellite altimeter missions are used in this paper (Figure 2). These missions include TOPEX/Poseidon (TP), Jason-1/Jason-2/Jason-3, the European Remote Sensing satellites ERS-1 and ERS-2 and the Environmental Satellite Envisat

21699291, 2020, 11, Downloaded from https://agupubs.onlinelibrary.wiley.com/doi/10.1029/2020JC016554 by University Of Washington, Wiley Online Library on [15/09/2025]. See the Terms and Conditions (https://onlinelibrary.wiley.com/terms-and-conditions) on Wiley Online Library for rules of use; OA articles are governed by the applicable Creative Commons License

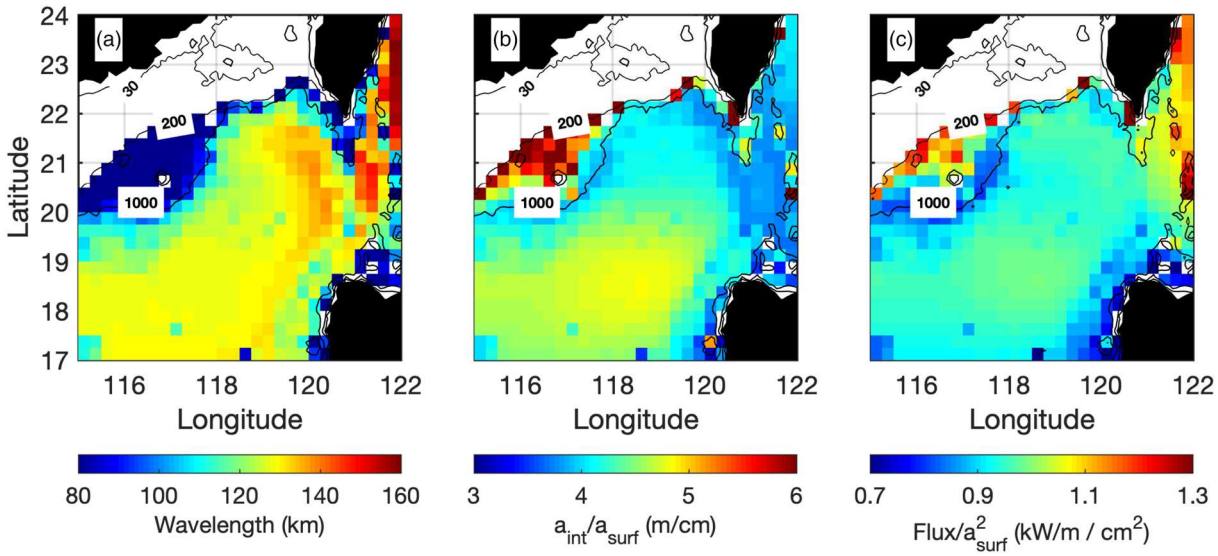

Figure 3. Parameters of the Mode-1 M_2 internal tide computed from climatological annual-mean hydrography in WOA2013. (a) Wavelength. (b) The transfer function from sea surface amplitude (a_{surf}) to internal amplitude (a_{int}). (c) The transfer function from sea surface amplitude (a_{surf}) to the depth-integrated energy flux.

(collectively referred to as ERS), and Geosat Follow-On (GFO). The data are produced by AVISO (Archiving, Validation, and Interpretation of Satellite Oceanographic Data) and distributed by CMEMS (Copernicus Marine Environment Monitoring Service). The data have been processed by applying standard corrections for atmospheric effects, surface wave biases, and geophysical effects. Data from different altimeter missions have different spatial sampling patterns (Figure 2a). There are 254, 488, and 1,002 ground tracks for TP (Jason-1/Jason-2/Jason-3), GFO, and ERS, respectively. The merged data set has higher spatial resolution, which is key for mapping internal tides of 100- to 200-km wavelength. The multisatellite measurements range from 1992–2018, with different missions having different time coverages (Figure 2c). The data set is labeled as MultiSat26yr in this study. The resultant internal tides represent the 26-year-long temporally coherent component, while the time-varying component is not tackled here (Zaron, 2017). The data set is larger than that used in a previous work in this region (Zhao, 2014).

2.2. Parameters and Transfer Functions

It is necessary to estimate internal tide properties, such as internal amplitude and energy flux, from satellite-observed sea surface amplitude (Zhao et al., 2016). Internal tides consist of a set of orthogonal dynamics modes, each of which has its characteristic modal structure in the vertical and freely propagates in the horizontal like a wave in a homogeneous fluid. The modal structures $\Phi_n(z)$ and eigenvalue speeds C_n^e can be determined from the Sturm-Liouville equation (Gill, 1982)

$$\frac{d^2\Phi_n(z)}{dz^2} + \frac{N^2(z)}{Cn^{e2}} = 0, \tag{1}$$

subject to boundary conditions $\Phi_n(0) = \Phi_n(-H) = 0$, where $N(z)$ is the stratification profile, H the ocean depth, and n the mode number. Assuming free-surface condition yields similar modal structure and a little higher C_n^e (Kelly, 2016). In this study, the stratification profile is from the climatological hydrography in the World Ocean Atlas 2013 (WOA2013) (Locarnini et al., 2013; Zweng et al., 2013). The ocean depth is from the 1-arc-min topography database developed using in situ and satellite measurements (Smith & Sandwell, 1997). With the Earth's rotation, phase speeds C_n^p differ from eigenvalue speeds and can be derived following $C_n^p = \omega C_n^e / \sqrt{\omega^2 - f^2}$, where ω and f are the tidal and inertial frequencies, respectively. From phase speeds and the tidal frequency, it is straightforward to calculate wavelengths and wave numbers. Figure 3a shows the wavelength of Mode-1 M_2 internal tides in the northeastern SCS ranging 115–122°E, 17–24°N. The theoretical wave number is one parameter used by plane wave analysis in mapping internal tides (section 2.3).

21699291, 2020, 11, Downloaded from https://agupubs.onlinelibrary.wiley.com/doi/10.1029/2020JC016554 by University Of Washington, Wiley Online Library on [15/09/2025]. See the Terms and Conditions (https://onlinelibrary.wiley.com/terms-and-conditions) on Wiley Online Library for rules of use; OA articles are governed by the applicable Creative Commons License

Table 1
Parameters Used in Mapping Mode-1 Internal Tides From Satellite Altimeter Data

Parameter	Value
Longitudinal range	115–122°E
Latitudinal range	17–24°N
Fitting window	150 km (M_2, O_1, K_1); 250 km (S_2)
Number of waves	3
Spatial grid	0.1° lon by 0.1° lat

Two transfer functions are presented here. The derivation process is omitted here to avoid repetition. Interested readers may refer to Zhao et al. (2016) for details. First, the sea surface amplitude a_{surf} of internal tides is calculated from sea surface pressure anomaly, which is the depth integration of internal amplitude a_{int}. The ratio of the surface to internal amplitudes ($a_{surf} : a_{int}$) is $1/g \int_{-H}^{0} N^2(z)\Phi(z)dz$. Figure 3b shows the ratio for the Mode-1 M_2 internal tide in the northeastern SCS. Generally, 1-cm sea surface amplitude is equivalent to 5-m internal amplitude. The second transfer function is from surface amplitude to the depth-integrated energy flux. It is a function of ocean depth, stratification, tidal frequency, and the inertial frequency. This transfer function is shown in Figure 3c and will be used to calculate the depth-integrated energy flux (section 2.4).

2.3. Methods

Plane wave analysis is a well-established technique for mapping internal tides from satellite altimetry. It has been employed to observe internal tide radiation from the Luzon Strait (Zhao, 2014). This technique determines internal tides from satellite altimeter data by fitting plane waves following $a\cos(Kx\cos\theta + Ky\sin\theta - \omega t - \phi)$, where ω and K are the frequency and wave number of the targeted internal tides, and a, θ, and ϕ are respectively amplitude, horizontal direction, and Greenwich phase to be determined. They are determined using all satellite SSH measurements SSH(x, y, t) in a fitting window by least squares fit. An iterative procedure has been developed to extract an arbitrary number of waves. This technique has the following advantages. (1) It maps internal tidal waves at regular grid from widely spaced satellite tracks. (2) Nontidal noise is significantly reduced by utilizing a large number of independent SSH data. (3) Internal tidal waves of different propagation directions are separately resolved.

This technique has been improved by combing with 2-D band-pass filtering (Zhao, 2019). The latter is key to further filter out nontidal noise, so that even weaker internal tides can be observed. In this study, the improved mapping technique is applied to the northeastern SCS to detect the much weaker southward internal tides. A detailed description of the mapping procedure is as follows:

Step 1: Construct the M_2 internal tide field from along-track satellite data by plane wave analysis. Table 1 lists parameters using in this step. The fitting window is 150 km by 150 km. Small fitting windows are preferred for high spatial resolution but limited by sparse ground tracks (Figure 2a). Larger windows (170, 190, 210, 230, and 250 km) are used to map the internal tide field repeatedly. All the results have similar spatial patterns but slightly different amplitudes. Thus, the size of fitting window does not affect the resultant internal tides qualitatively. In each window, three largest waves are extracted and their sum gives the internal tide at the center of the window. More waves with decreasing amplitudes can be determined iteratively in this step; however, those low-amplitude waves can be neglected without affecting the final internal tide field. Plane wave analysis is conducted in overlapping windows at 0.1° by 0.1° regular grid. The prerequisite parameter of wave number is from WOA2013 (section 2.2; Figure 3a). Internal tides in water <1,000 m deep are discarded. Figure 4a shows the resultant M_2 internal tide field.

Step 2: Clean the M_2 internal tide field by 2-D band-pass filtering. The above constructed M_2 internal tide field can be cleaned using theoretical wave number. Figure 4b shows the 2-D wave number spectrum of the internal tide field in Figure 4a. The spectrum is band-pass filtered using the theoretical wave number. In Figure 4b, the dotted circle shows the theoretical wave number. The solid circles give the cutoff wave numbers, which are taken as [0.8 1.25] times the theoretical wave number. The broadband 2-D filter is to account for the variation of wavelength in both time and space. The band-pass-filtered spectrum is converted back to the physical space by inverse Fourier transform (Figure 4c). It is evident that the spatially filtered field is clean and smooth. The removed nontidal noise is given Figure 4d.

Step 3: Decompose the M_2 internal tide field by plane wave analysis. In this step, plane wave analysis is called again to decompose the filtered internal tide field. It uses the same parameters listed in Table 1. The input is the 2-D filtered internal tide field shown in Figure 4c. Plane wave analysis is able to separately resolve multiple internal tidal waves of different propagation directions and thus

21699291, 2020, 11, Downloaded from https://agupubs.onlinelibrary.wiley.com/doi/10.1029/2020JC016554 by University Of Washington, Wiley Online Library on [15/09/2025]. See the Terms and Conditions (https://onlinelibrary.wiley.com/terms-and-conditions) on Wiley Online Library for rules of use; OA articles are governed by the applicable Creative Commons License

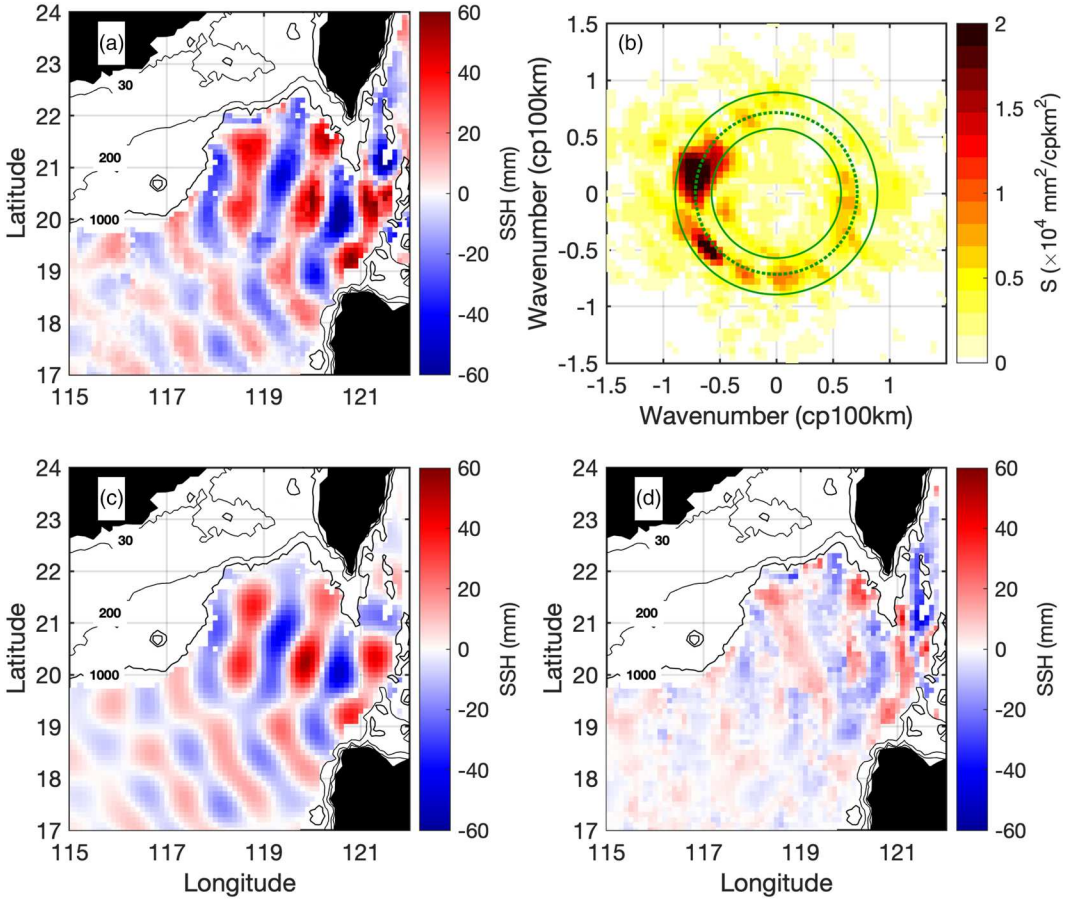

Figure 4. Mapping the Mode-1 M_2 internal tide from satellite altimetry. (a) The M_2 internal tide field constructed from along-track altimeter data by plane wave analysis. (b) Two-dimensional wave number spectrum of (a). The dotted-line circle indicates the theoretical wave number. The solid-line circles indicate the filter's cutoff wave numbers. They are [4/5 5/4] times the theoretical wave number. (c) The M_2 internal tide field after 2-D band-pass filtering. (d) Nontidal noise removed in this step, that is, the difference between (a) and (c).

resolves multiwave interference. In the end, there are three internal waves at each grid point. The results will be examined in the following sections.

2.4. Multiwave Decomposition

In this section, I first examine the directionality of the internal tide field and then divide it into three components by direction. Figure 5a shows the 2-D wave number spectrum of the final three-wave-summed internal tide field. It gives variance distribution in the wave number domain. As expected, the variance is mainly around the theoretical wave number (green circle). Figure 5a is much cleaner than the spectrum of the first-round internal tide field shown in Figure 4b, because the field has been further cleaned by 2-D filtering in Step 2. Figure 5b shows the rosette of propagation directions of all individual waves. Its lobes indicate the dominant propagation directions of internal tides in this region. Figures 5a and 5b give the same directionality of the internal tide field. Both reveal two dominant propagation directions along 165° and 220°, respectively. They are the northwestward and southwestward internal tides from the Luzon Strait (Zhao, 2014). Figures 5a and 5b both reveal the presence of weak southward internal tides and even weaker eastward internal tides.

Then I divide the internal tide field into three components by propagation direction (Figure 5). They are the westward (90–240°), southward (240–320°), and eastward components (−40–90°), respectively. Their directional ranges are bounded by the blue lines. In fact, the westward and southward components are internal tides originated in the Luzon Strait and on the continental slope, respectively. By this way, internal

21699291, 2020, 11, Downloaded from https://agupubs.onlinelibrary.wiley.com/doi/10.1029/2020JC016554 by University Of Washington, Wiley Online Library on [15/09/2025]. See the Terms and Conditions (https://onlinelibrary.wiley.com/terms-and-conditions) on Wiley Online Library for rules of use; OA articles are governed by the applicable Creative Commons License

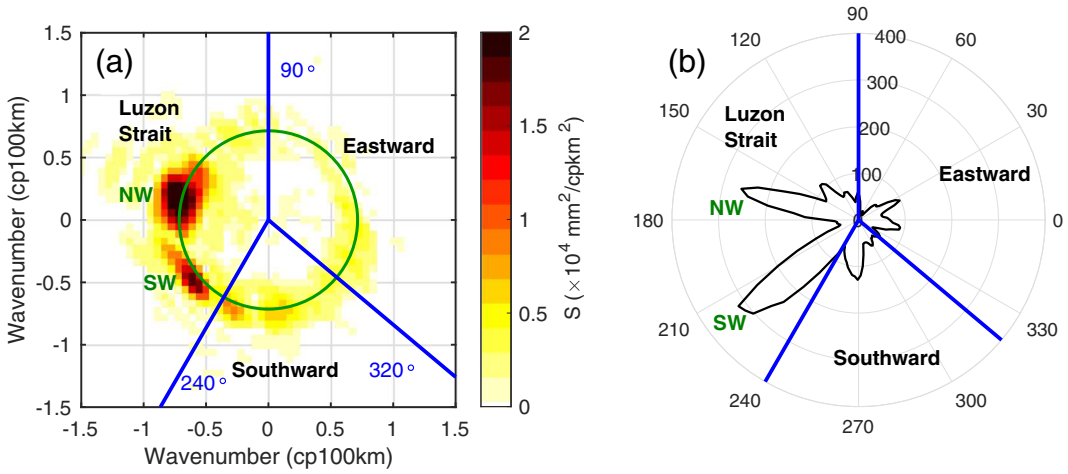

Figure 5. Directionality of the final internal tide field. (a) Two-dimensional wave number spectrum. (b) Rosette of propagation directions of all internal tidal waves. The internal tide field is decomposed into three components bounded by blue lines: the Luzon Strait component (90–240°), the southward component (240–320°), and the eastward component (−40–90°). The Luzon Strait component has two internal tidal beams: northwestward (NW, 165°) and southwestward (SW, 220°).

tides from different generation sites are separately resolved. The decomposition of multidirectional waves is one advantage of plane wave analysis over pointwise harmonic analysis.

Figure 6a shows the newly constructed M_2 internal tide field. Its three components are shown in Figures 6b–6d, respectively. The decomposed components are self-evident. For example, the internal tides from both generation sits have smooth phase and wavefront, in contrast to the multiwave interfered field in Figure 6a. Among them, the internal tides from the Luzon Strait have been reported previously in Zhao (2014), who has observed the northwestward (165°) and southwestward (220°) beams. This bifurcation can be clearly seen in the internal tide field (Figure 6b). The two beams are generally from the northern and southern sections of the Luzon Strait (green line). Figure 6d shows eastward internal tides. Considering their coherent spatial pattern, I suggest that they are real (not artificial) signals, though their generation needs further investigation.

The depth-integrated energy fluxes are computed from the satellite-observed SSH amplitudes, using the transfer function explained in section 2.2 and Figure 3c. The flux direction is the direction of the wave determined in plane wave analysis. The energy fluxes (propagation directions) confirm that the internal tides propagate away from the two different generation sites. This feature confirms the multiwave decomposition method. The decomposed fields make it possible to better understand their generation and propagation.

3. Evaluations

3.1. Evaluation of the Method

The new mapping technique combines plane wave analysis and 2-D spatial filtering. The role of the 2-D spatial filtering is evaluated here by comparing internal tides obtained in the first- and second-round plane wave analysis (Figure 7). It compares both of the westward and southward components. Obviously, the second-round internal tide fields are much cleaner and smoother, particularly for the weak southward internal tides. The first-round results may suggest southward internal tides, but inconclusive (Figure 7b). They are distorted by the larger westward internal tides (Figure 7c) and energetic mesoscale eddies. After 2-D spatial filtering, the weak southward internal tides are evident and conclusive: smooth phase, uniform flux, and clean wavefront. Comparing Figures 7a and 7c, one can also see improvements in the westward Luzon Strait internal tides. To conclude, the detectability of the southward internal tides benefits from the newly developed mapping technique.

3.2. Evaluation of the Result

Independent CryoSat-2 SSH measurements are used to evaluate the internal tides extracted from Multi-Sat26yr (Figure 2). The CryoSat-2 data are exactly 9 years long from January 2010 to January 2019. CryoSat-2

21699291, 2020, 11, Downloaded from https://agupubs.onlinelibrary.wiley.com/doi/10.1029/2020JC016554 by University Of Washington, Wiley Online Library on [15/09/2025]. See the Terms and Conditions (https://onlinelibrary.wiley.com/terms-and-conditions) on Wiley Online Library for rules of use; OA articles are governed by the applicable Creative Commons License

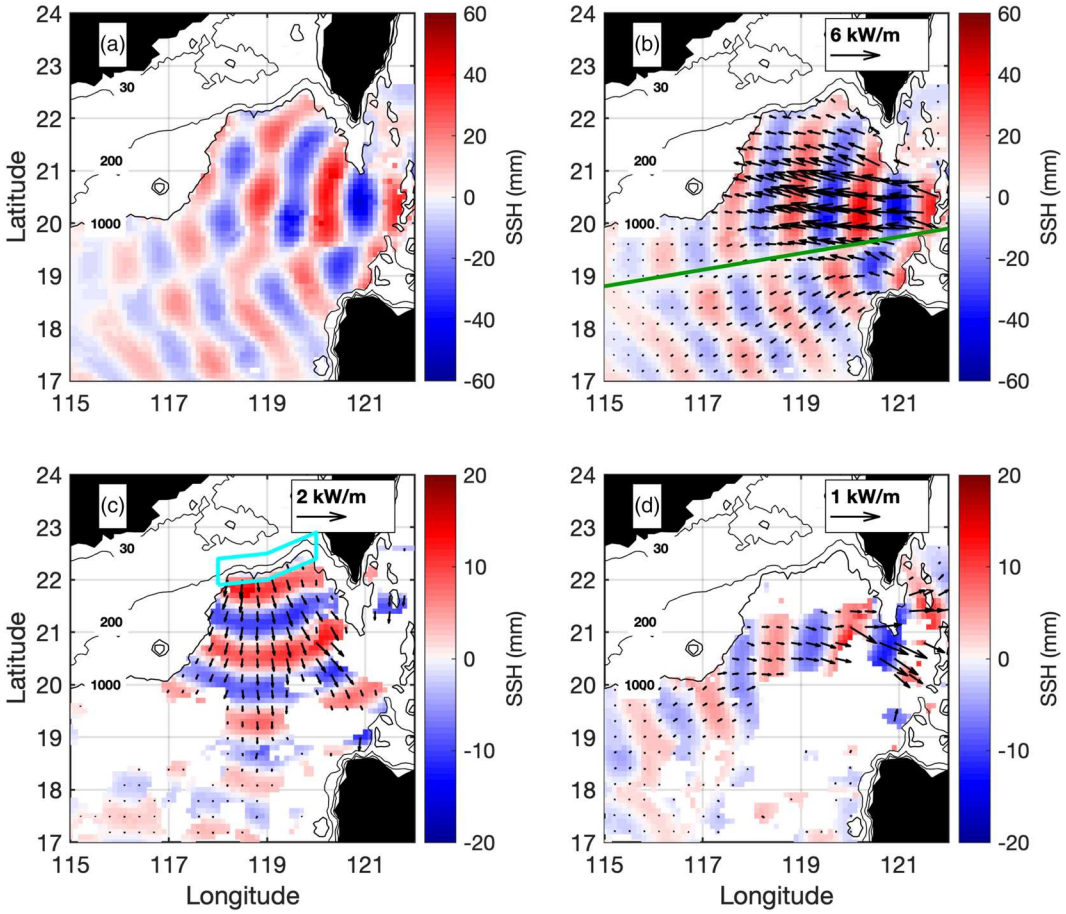

Figure 6. Decomposition of the M_2 internal tides field in the northeastern SCS. (a) The three-wave-summed internal tide field. (b) The Luzon Strait component (90–240°). The northwestward and southwestward beams are separated by the green line. (c) The southward component (240–320°). (d) The eastward component (−40–90°). Black arrows in (b)–(d) are the depth-integrated energy fluxes. Black lines indicate isobathic contours of 30, 200, and 1,000 m, respectively.

is a long-repeat-track mission. It has a repeat cycle of 369 days and 10,688 ground tracks (Wingham et al., 2006). It has 8-km intertrack spacing and thus uniform spatial distribution (Figure 2b). The data have been corrected for atmospheric effects, surface wave biases, and geophysical effects in the same manner (section 2.1). The CryoSat-2 data have been previously used for evaluating empirical internal tide models developed using multisatellite data collected by exact-repeat-track altimeter missions (Ray & Zaron, 2016; Zaron, 2019; Zhao, 2019) and mapping M_2 internal tides (Zhao, 2016). In contrast, pointwise mooring measurements at individual stations are not well qualified for assessing empirical internal tide models, because moorings cannot resolve multidirectional waves and thus are subjected to complicated temporal and spatial variations.

The M_2 internal tides model developed in section 2 is used to predict and remove internal tides in the CryoSat-2 data, and its performance is indicated by SSH variance reduction. The procedure is as follows. For all CryoSat-2 SSH measurements with known locations and times, the internal tide signals are predicted using the model developed in section 2. The predicted internal tide signals are subtracted from corresponding CryoSat-2 data. The SSH variance is calculated before and after the internal tide correction, and their difference is variance reduction. In this study, the pointwise variance values are binned into overlapping 2° by 2° windows at regular grid of 1° longitude by 1° latitude. Figure 8 illustrates the model evaluation. The CryoSat-2 SSH variance prior to internal tide correction is shown in Figure 8a. The variance reduction is shown in Figure 8b. The reduction values are mostly positive, suggesting that the model can remove internal tides and thus reduce variance in the CryoSat-2 data. The model's variance is shown in Figure 8d. Figures 8b and 8d have similar spatial patterns, justifying the evaluation method. Figure 8c shows the ratio of the

21699291, 2020, 11, Downloaded from https://agupubs.onlinelibrary.wiley.com/doi/10.1029/2020JC016554 by University Of Washington, Wiley Online Library on [15/09/2025]. See the Terms and Conditions (https://onlinelibrary.wiley.com/terms-and-conditions) on Wiley Online Library for rules of use; OA articles are governed by the applicable Creative Commons License

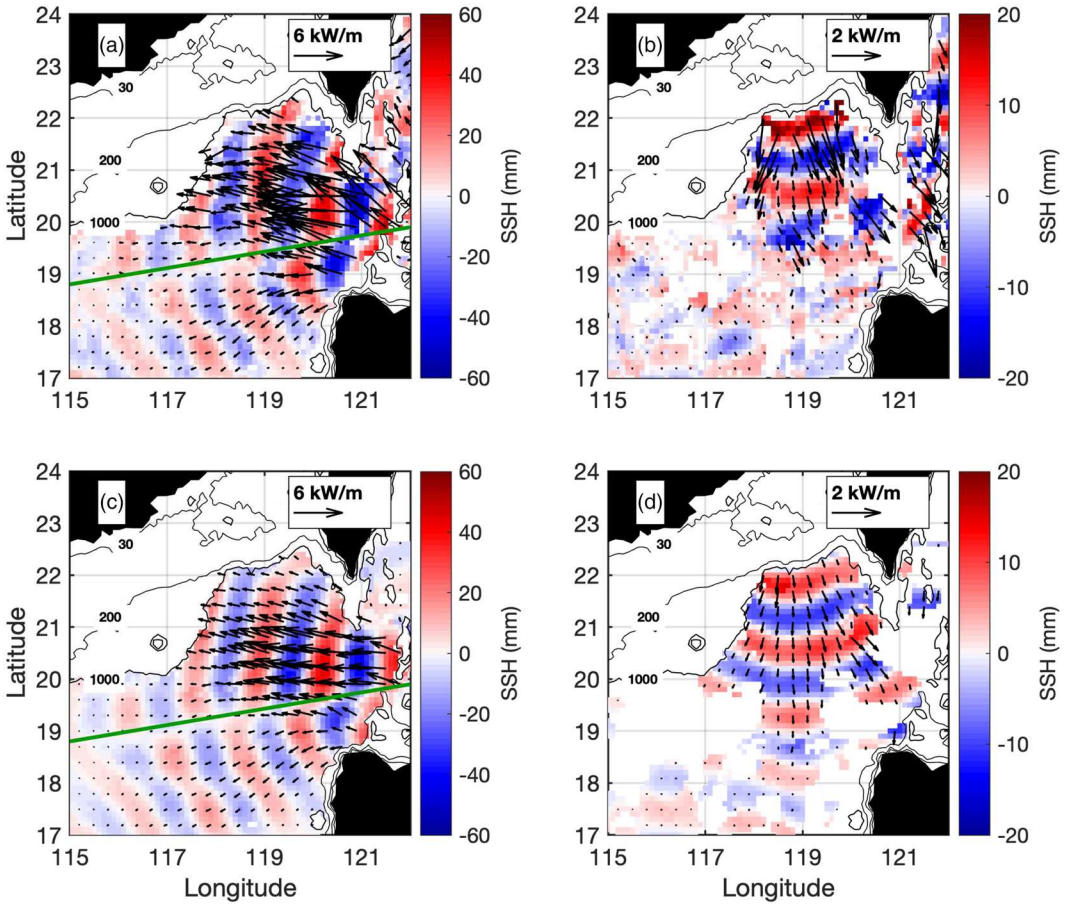

Figure 7. Comparison of M_2 internal tides obtained in the first- and second-round plane wave analysis. (a, b) The first round. (c, d) The second round as in Figures 6b and 6c. (a, c) The Luzon Strait component. (b, d) The southward component. Black arrows are the depth-integrated energy fluxes. Black lines indicate isobathic contours of 30, 200, and 1,000 m, respectively.

variance reduction to the raw variance. It shows that the internal tide's variance is generally lower than 5%. The largest percentage up to 15% occurs to the west of the Luzon Strait, where energetic internal tides are well known (see section 1). To conclude, the internal tide field from MultiSat26yr is reliable.

4. Internal Tides From the Continental Slope

4.1. Southward Internal Tides

This study reveals a clear picture of the southward M_2 internal tides from the continental slope at the southern entrance to the Taiwan Strait (Figure 6). The internal tides start from the continental slope along 22°N ranging 118–120°E. They propagate southward for about 300 km from 22°N to 19°N. In propagation, the tidal beam slightly spreads, and its width increases from 200 km at 22°N to about 400 km at 20°N. The southward internal tides have maximum SSH amplitudes about 10 mm, much lower than the 50-mm amplitudes of the northwestward internal tides from the Luzon Strait. The internal amplitudes can be computed using the transfer function in Figure 3b. Here the 10-mm SSH amplitude is equivalent to a 5-m internal amplitude (peak-to-peak amplitude 10 m). The recognition of this weak beam benefits from the improved mapping technique. This is for the first time the 300-km-long southward M_2 internal tidal beam in the northeastern South China Sea is reported.

The depth-integrated fluxes are shown as black arrows in Figures 6. These vectors point away from their respective generation sites. The total energy fluxes are obtained by integrating fluxes across these beams. The total westward flux from the Luzon Strait is 1.8 GW. It is slightly greater than 1.5 GW reported in Zhao (2014). The slight increase is likely due to the smaller fitting window (150 km vs. 200 km). The integrated southward

21699291, 2020, 11, Downloaded from https://agupubs.onlinelibrary.wiley.com/doi/10.1029/2020JC016554 by University Of Washington, Wiley Online Library on [15/09/2025]. See the Terms and Conditions (https://onlinelibrary.wiley.com/terms-and-conditions) on Wiley Online Library for rules of use; OA articles are governed by the applicable Creative Commons License

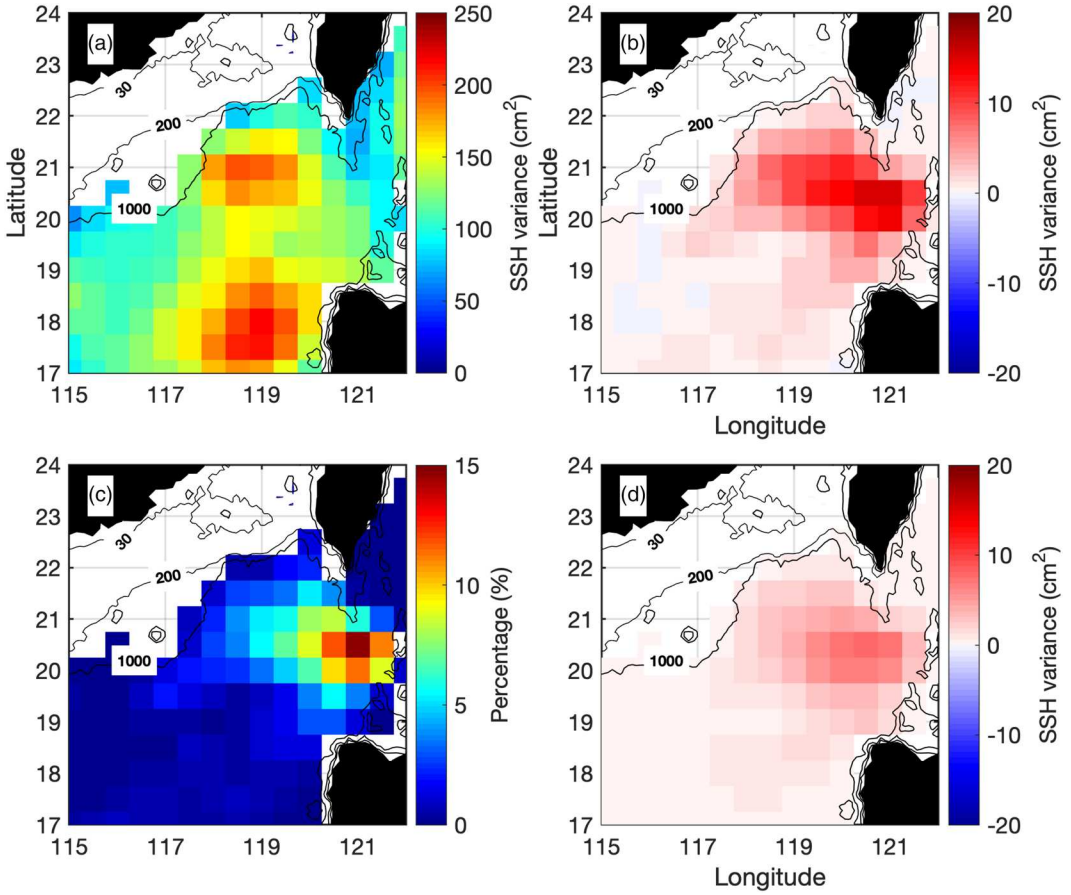

Figure 8. Evaluation of the M_2 internal tide model using independent CryoSat-2 data. (a) Variance of the raw CryoSat-2 data. (b) Variance reduction by internal tide correction. (c) Percentage of the variance reduction. It is the ratio of (b) to (a). (d) Variance of the M_2 internal tide model.

flux is 0.18 GW, about 10% of the westward Luzon Strait flux. Note that both are low-bound values, because they are the 26-year-long coherent results. It is well known that internal tides lose coherence due to the time-varying ocean environment (Ray & Zaron, 2011; Zaron, 2015, 2017). For the Luzon Strait internal tides, Zhao (2014) compares the satellite-derived energy fluxes with those by numerical models, and finds that the former is about 50% of the latter. Assuming this relation holds for internal tides generated on the continental slope, the southward energy flux will be ~0.36 GW.

4.2. Generation Site

The southward internal tides start from the steep continental slope, suggesting that the continental slope is their source region. This hypothesis is testified in this section. The barotropic tide in this region has been well studied previously by tide gauges, numerical models, and satellite altimetry (Egbert & Erofeeva, 2002; Yu et al., 2017; Zu et al., 2008). The model results here are predicted from TPXO.8 (Egbert & Erofeeva, 2002). Figure 9a shows that the M_2 tide enters the Taiwan Strait mainly via its northern entrance in the East China Sea (ECS) and its southern entrance in the SCS. The M_2 tidal amplitude is up to 2 m due to the superposition of the southward and northward waves (Figure 9a). Strong tidal currents mainly occur in the southern strait (Figure 9b). In particular, on the continental slope, the tidal currents are largely perpendicular to the isobathic contours (Figure 9b), favoring internal tide generation.

The generation site can be further examined by the barotropic tide body force $F = Q \cdot \nabla H \cdot N_b^2/\omega$, where Q is the barotropic tidal transport from TPXO.8, ∇H is bottom gradient, N_b^2 is stratification above bottom from WOA2013, and ω is the M_2 tidal frequency. The bottom depths are from the 1-arc-min topography database (Smith & Sandwell, 1997). Figure 9c shows the barotropic tide body force. The spatial pattern agrees with previous studies very well (Bai et al., 2014; Jan et al., 2008). It reveals strong conversion on the steep

21699291, 2020, 11, Downloaded from https://agupubs.onlinelibrary.wiley.com/doi/10.1029/2020JC016554 by University Of Washington, Wiley Online Library on [15/09/2025]. See the Terms and Conditions (https://onlinelibrary.wiley.com/terms-and-conditions) on Wiley Online Library for rules of use; OA articles are governed by the applicable Creative Commons License

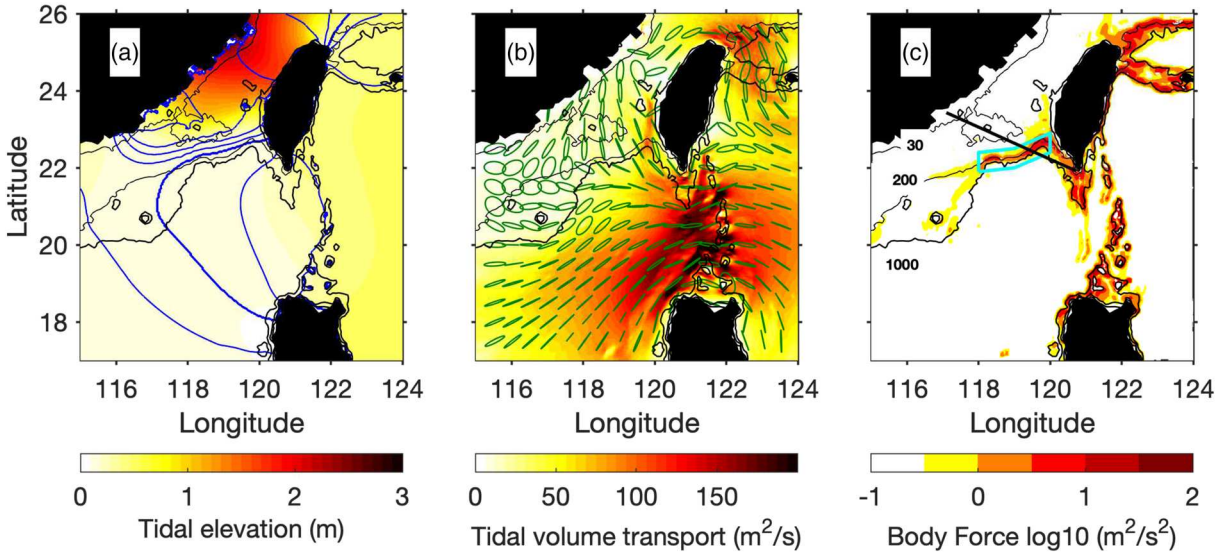

Figure 9. M_2 barotropic tide from TPXO.8 and body force. (a) Tidal amplitude. Blue lines indicate the Greenwich co-phase chart with intervals of 30°, with 0° co-phase lines being in bold. (b) Volume transport and tidal ellipses. Tidal ellipses (with major axes scaled to unit) are shown in green at grid of 0.5° longitude by 0.5° latitude. (c) Barotropic tidal body force in the logarithmic scale. In all panels, black lines indicate isobathic contours of 30, 200, and 1,000 m, respectively. The cyan boxes indicate the generation site on the continental slope. The thick black line in (c) indicates the boundary between the South China Sea and the Taiwan Strait.

continental slope at the southern entrance to the southern Taiwan Strait (cyan box). The body force shows that the generation is on the narrow steep continental slope ranging from 118–120°E along 22°N.

Figure 9c shows that the local internal tide generation on the continental slope near Dongsha is about 2 orders of magnitude weaker. It is unlikely that the eastward internal tides are locally generated. I think they are reflected internal tides off the continental slope, consistent with previous analysis by Klymak et al. (2011). The incident westward internal tides from the Luzon Strait may partially reflect on the continental slope. As shown in this study, it is difficult to resolve the even weaker reflected internal tides. Fortunately, the new satellite result presented in this study offers a feasible avenue to explore this process.

4.3. Internal Tides and ISWs

This section explores the causative relation of internal tides and ISWs in this region. It is well known that ISWs near Dongsha are from nonlinear steepening of internal tides (Alford et al., 2015; Zhang et al., 2011; Zhao, 2014; Zhao et al., 2004). This relation has been confirmed by field measurement, satellite observations and numerical models. Here Figure 10a illustrates this relation by their spatial distribution. Figure 10a shows the westward internal tides, superimposed with ISWs in Zhao et al. (2004) and Bai et al. (2014). One can see that the ISWs and the internal tidal wavefronts agree with each other.

Bai et al. (2014) report that ISWs are frequently observed in the southern Taiwan Strait and suggest that these ISWs may be generated either by local tide-bottom interaction or by incident internal tides from the Luzon Strait. Bai et al. (2019) further confirm that the onshore propagation of internal tides and ISWs by field measurements to the south of Taiwan Bank. Min et al. (2019) simulate the generation of ISWs from these two sources using a 2-D nonhydrostatic numerical model. Figure 10b show the southward internal tides, superimposed with satellite-observed ISWs. These onshore propagating ISWs are located on the continental shelf, to the north of the steep continental slope. The southward internal tides are located to the south of the slope. This feature suggests that their common generation source is the continental slope. This scenario suggests that the tide-bottom interaction on the continental slope has two components. The onshore component propagates into shallow water and induces ISWs, due to shoaling bottom and nonlinear steepening. The offshore component propagates into deep water in the form of linear internal tides. In this study, the southward internal tides in the deep water are observed by satellite altimetry.

Both the Luzon Strait and the steep continental slope generate internal tides. But they are very different. In the Luzon Strait, strong barotropic tide propagates from the western Pacific into the SCS. Internal tides are generated while barotropic tidal flows over the ridges and scatters energy into internal tides. The

21699291, 2020, 11, Downloaded from https://agupubs.onlinelibrary.wiley.com/doi/10.1029/2020JC016554 by University Of Washington, Wiley Online Library on [15/09/2025]. See the Terms and Conditions (https://onlinelibrary.wiley.com/terms-and-conditions) on Wiley Online Library for rules of use; OA articles are governed by the applicable Creative Commons License

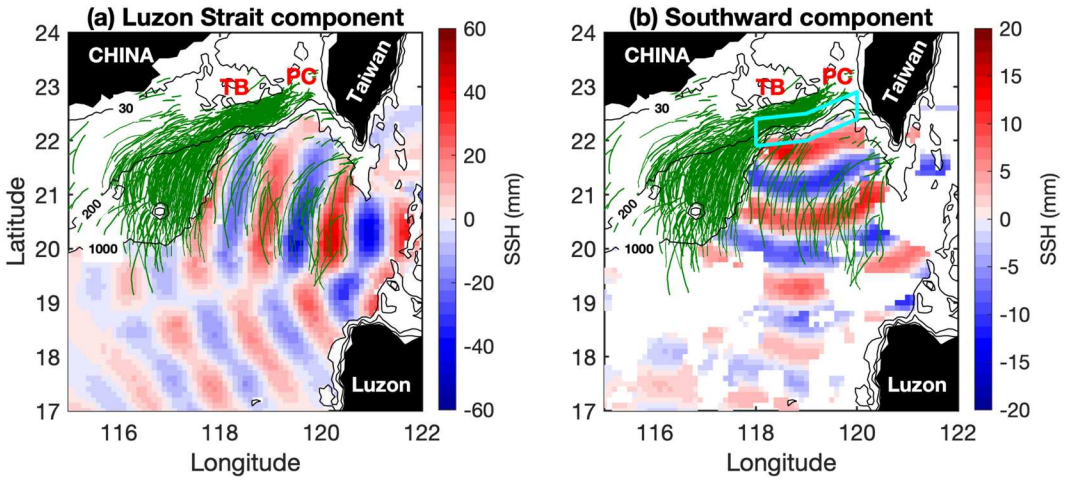

Figure 10. Internal tides and internal solitary waves (ISWs) in the northeastern SCS. (a) The westward M_2 internal tides from the Luzon Strait. (b) The southward M_2 internal tides from the continental slope. The green lines indicate ISWs observed by Zhao et al. (2004) and Bai et al. (2014). The black lines indicate isobathic contours of 30, 200, and 1,000 m, respectively. The cyan box indicates the generation site on the continental slope. Taiwan Bank (TB) and Penghu Channel (PC) are labeled.

back and forth tidal current generates both eastward and westward internal tides (Zhao, 2014). In contrast, at the southern entrance to the Taiwan Strait, the barotropic to baroclinic tidal conversion occurs on the steep continental slope. The onshore radiation evolves into ISWs and the offshore radiation appears as internal tides.

5. Spatial Variability Due to Multiwave Interference

The northeastern SCS contains multiple internal tides of different propagation directions. It is dominated by northwestward internal tides from the Luzon Strait and also affected by southward internal tides from the continental slope. The superposition of two internal tidal beams forms constructive and destructive zones, depending on their phase difference. The energy flux in a multiwave field is spatially variable. The energy flux can be calculated from the internal tide's pressure p' and velocity U' following $< p'U' >$, where the brackets denote the mean in time. Note that U' has a transverse component following $v = u * f/\omega$, where f and ω are the near-inertial and tidal frequencies, respectively. To demonstrate the spatial variability due to mutliwave interference, two plane waves and their superposition are constructed. The SSH amplitude and propagation direction of the northwestward wave are 30 mm and 165°, respectively (Figure 11a). Those of the southward wave are 10 mm and 270°, respectively (Figure 11b). These values are chosen from the above satellite altimetric observations (Figures 6). Other parameters (stratification, modal structure, and inertial frequency) are adopted from the WOA2013 stratification profile at 20°N, 119°E. The calculation method is described in Zhao et al. (2010). The arrows in Figures 11a and 11b show energy fluxes for these two internal waves. Figures 11d and 11e show their flux magnitudes and directions along one section (green lines). The ratio of their flux magnitudes is about 1:9, consists with their amplitude ratio of 1:3. Neither of these two internal wave fields show spatial variations in magnitude and direction.

The superposition of these two internal tidal waves is given in Figures 11c and 11f. Figure 11c shows the superposed SSH field and pointwise energy fluxes. Figure 11f shows the values along the same green line. The results show significant spatial variations in flux magnitude and direction, although the southward wave is much weaker. The resultant propagation direction may vary by ±20° around the direction of the northwestward wave (165°). The largest flux may be two times the lowest value. Similar features have been observed using field measurements in other regions (Johnston et al., 2015; Martini et al., 2007; Nash et al., 2006; Rainville et al., 2010; Wang et al., 2018; Zhao et al., 2010). In other words, the dominant northwestward internal tides from the Luzon Strait are significantly modulated by the much weaker southward internal tides. The superposition causes significant spatial variations in flux magnitude and direction. Such an interference pattern means large differences in mooring measurements at different sites. In order to better study the propagation and dissipation of internal tides, the multiwave interference field should be decomposed

21699291, 2020, 11, Downloaded from https://agupubs.onlinelibrary.wiley.com/doi/10.1029/2020JC016554 by University Of Washington, Wiley Online Library on [15/09/2025]. See the Terms and Conditions (https://onlinelibrary.wiley.com/terms-and-conditions) on Wiley Online Library for rules of use; OA articles are governed by the applicable Creative Commons License

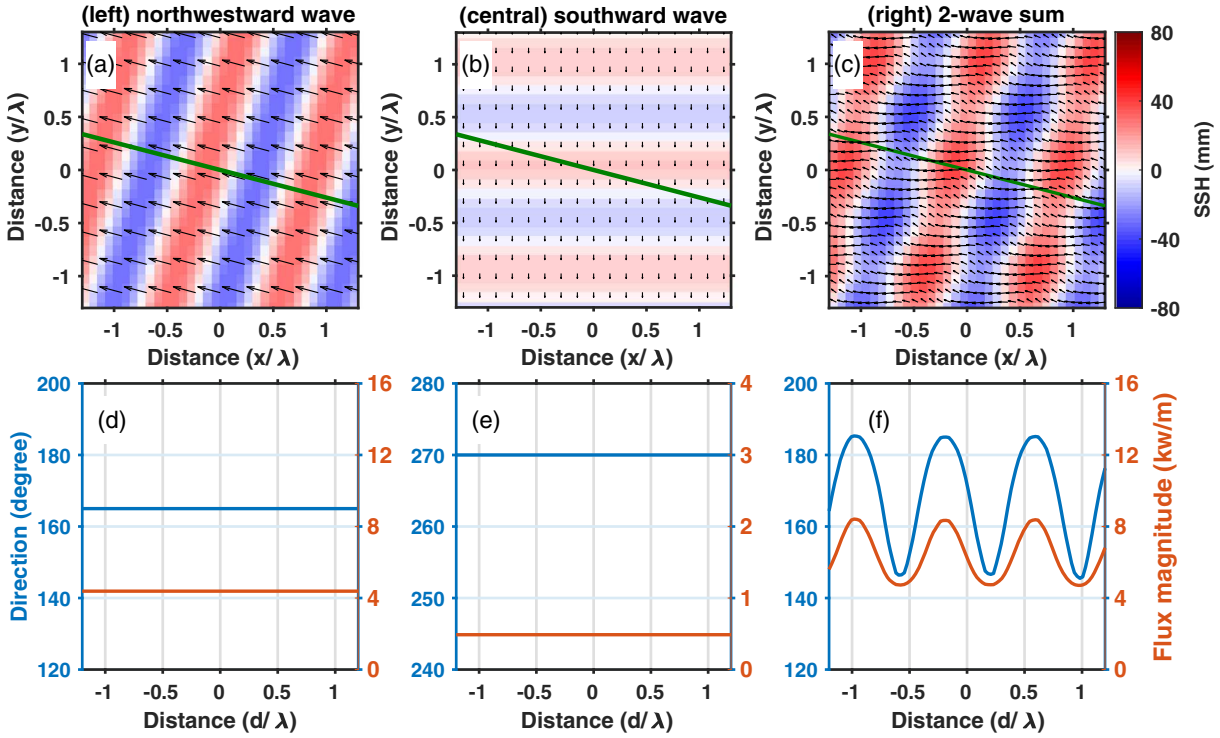

Figure 11. Interference of two mode-1 M_2 internal tidal waves. (left panels) Northwestward internal tide (SSH amplitude = 30 mm; propagation direction = 165°). (a) Colors indicate a snapshot SSH field. Arrows indicate depth-integrated energy fluxes. (d) Magnitude and propagation direction of energy fluxes along the green line in (a). (central panels) As in left panels but for a southward internal tide (SSH amplitude = 10 mm; propagation direction = 270°). (right panels) The superposition of the northwestward and southward internal tidal waves. In all panels, the distance axes are normalized by one wavelength (λ). The stratification profile and parameters used in the calculation are from 20°N, 119°E in WOA2013.

into individual waves of different propagation directions. Then these dynamic processes can be studied along individual long-range internal tidal beams. This paper describes a decomposition technique that can be applied to other study regions.

Recent studies using mooring measurements reveal strong variations of internal tides caused by the Kuroshio intrusion, seasonal stratification, and mesoscale eddies (Huang et al., 2018; Li et al., 2016; Park & Farmer, 2013; Zaron, 2017). Here I further show that the multiwave superposition may lead to significant spatial variations. To study the spatiotemporal variation of internal tides, it is necessary to distinguish the variations caused by ocean dynamic processes and by multiwave interference. The proper approach is separately resolving internal tides of different propagation directions using the method presented in this paper.

6. Semidiurnal and Diurnal Internal Tides

In this study, the new mapping technique has been applied to three more tidal constituents (S_2, O_1, and K_1) to see whether they have southward beams from the continental slope. The results are presented in this section. Based on all these results, I find that the steep continental slope radiates southward semidiurnal M_2 and S_2 internal tides, but no southward diurnal O_1 and K_1 internal tides.

6.1. S_2 Internal Tides

The S_2 internal tides are investigated following the same procedure. The prerequisite S_2 parameters and transfer functions are calculated as for M_2. Due to tidal aliasing, the ERS data cannot detect the S_2 internal tides. The reduced data set has even sparse ground tracks (Figure 12a, green dots); therefore, larger squared fitting windows of 250 km one side are used for S_2, in contrast to 150 km for M_2. Additionally, the amplitudes of the S_2 internal tides are about 40% those of M_2, making it more challenging to observe S_2 by satellite altimetry. The S_2 internal tides in this region have not been addressed in previous studies (Zhao, 2014). This gap of knowledge is filled in this paper.

21699291, 2020, 11, Downloaded from https://agupubs.onlinelibrary.wiley.com/doi/10.1029/2020JC016554 by University Of Washington, Wiley Online Library on [15/09/2025]. See the Terms and Conditions (https://onlinelibrary.wiley.com/terms-and-conditions) on Wiley Online Library for rules of use; OA articles are governed by the applicable Creative Commons License

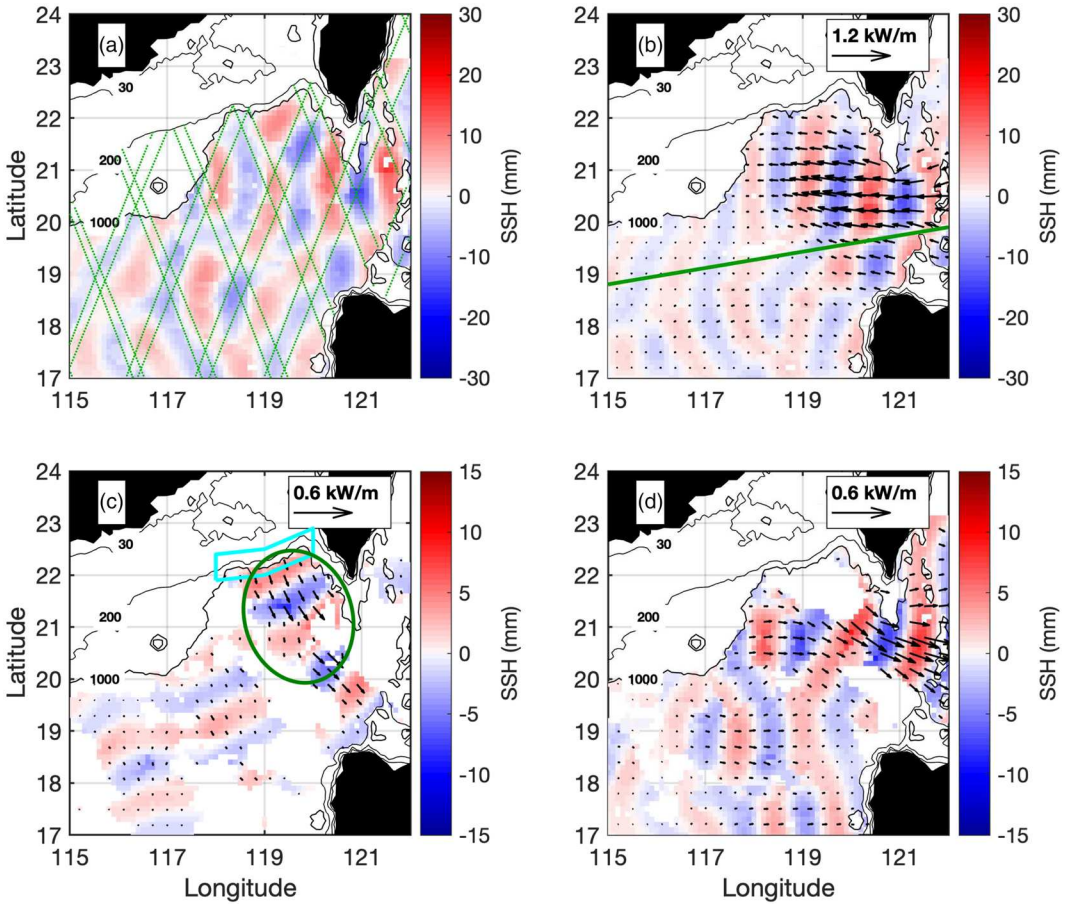

Figure 12. The S_2 internal tides in the northeastern SCS. (a) The three-wave summed internal tide field. The green dots indicate satellite along-track data points. (b) The Luzon Strait component (90–240°). The northwestward and southwestward beams are separated by the green line. (c) The southward component (240–320°). The cyan boxes indicate the generation site on the continental slope. (d) The eastward component (−40–90°). Black arrows in (b)–(d) are the depth-integrated energy fluxes. Black lines indicate isobathic contours of 30, 200, and 1,000 m, respectively.

Figure 12 shows the resultant S_2 internal tides, in the same format as Figure 6 for M_2. For the same reason, the S_2 field is divided into westward (90–240°), southward (240–340°), and eastward (−40–90°) components. Figure 12b shows northwestward and southwestward S_2 internal tides from the Luzon Strait (separated by the green line). Among them, the large northwestward internal tides are very clean, while the weak southwestward internal tides are visible though noisy. Figure 12d shows the eastward component. It may contain real internal tides and nontidal noise, and thus no conclusive information can be drawn. Figure 12c shows the southward component, which also hints southward radiation from the continental slope. One can see southeastward S_2 internal tides (green ellipse) from the steep continental slope. They become undetectable after one cycle. Although the fewer ground tracks, I suggest that they are real southward S_2 internal tides. Indeed, the M_2 and S_2 superposition gives spring-neap cycles, consistent with the temporal variations in internal tides and ISWs near Taiwan Bank (Bai et al., 2019). In summary, there are southward semidiurnal internal tides (M_2 and S_2) in the northeastern South China Sea.

6.2. K_1 and O_1 Internal Tides

The K_1 and O_1 internal tides are investigated following exactly the same mapping procedure as for M_2 (Figure 13). Their respective parameters and transfer functions are calculated as well. The diurnal internal tides have much longer wavelengths of 300–500 km, contrast with 100–150 km for the semidiurnal internal tides (Zhao, 2014). It is a challenge to extract the long-wavelength diurnal internal tides, because the generation stripe on the continental slope only ranges 200 km long from 118° to 120°E. Directionality analysis (not shown) reveals that the diurnal internal tides in this region are dominantly westward and eastward. Therefore, each of the K_1 and O_1 internal tide fields is divided into two components (Figure 13): eastward

21699291, 2020, 11, Downloaded from https://agupubs.onlinelibrary.wiley.com/doi/10.1029/2020JC016554 by University Of Washington, Wiley Online Library on [15/09/2025]. See the Terms and Conditions (https://onlinelibrary.wiley.com/terms-and-conditions) on Wiley Online Library for rules of use; OA articles are governed by the applicable Creative Commons License

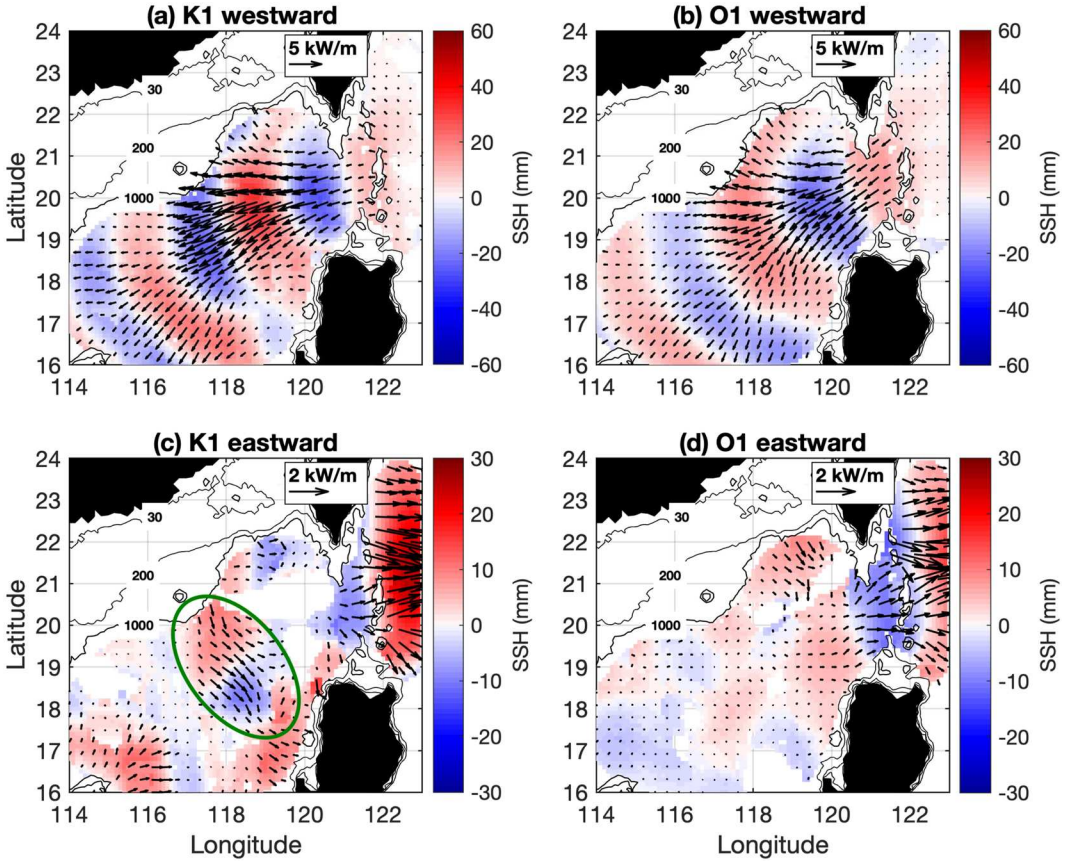

Figure 13. (a, c) K_1 and (b, d) O_1 internal tides in the northeastern SCS. (a, b) The westward component (90°–270°). (c, d) The eastward component (−90–90°). Black arrows are the depth-integrated energy fluxes. The black lines indicate isobathic contours of 30, 200, and 1,000 m, respectively. There are no significant southward diurnal internal tides from the northern continental slope.

(−90–90°) and westward (90–270°). Both tidal constituents show the prevailing westward radiation from the Luzon Strait. Their convex wavefronts suggest that they cylindrically spread in propagation. Also, their central paths bend equatorward due to the beta effect. To the east of the Luzon Strait, eastward internal tides can be clearly seen. These features are consistent with previous observations in Zhao (2014), but the new results are much clearer, thanks to the improved mapping technique. There are no southward diurnal internal tides from the continental slope. One can see spatially coherent southward K_1 internal tides from the continental slope near Dongsha (Figure 13c, green ellipse), which are likely reflected internal tides. The lack of southward diurnal internal tides is not a surprise, because the diurnal barotropic tidal currents are weak in the Taiwan Strait (Yu et al., 2017; Zu et al., 2008).

7. Summary

In this study, I have investigated the internal tides in the northeastern SCS using an improved mapping technique developed in Zhao (2019). The new mapping technique combines plane wave analysis with 2-D band-pass filtering that can further reduce nontidal noise (Figure 4). The new technique makes it possible to observe the much weaker southward internal tides in this region. The decomposed internal tide fields by propagation direction provide unprecedented details about the internal tide field (Figure 6). The mapping technique has been confirmed by comparing the first- and second-round fitted internal tide fields (Figure 7). The final internal tide field is evaluated and confirmed using independent CyroSat-2 data (Figure 8).

There exists strong barotropic to baroclinic tidal conversion on the steep continental slope at the southern entrance to the Taiwan Strait (Figure 9). The generation source ranges from 118° to 120°E along 22°N. The southward M_2 internal tides propagate about 300 km from 22° to 19°N in the northeastern SCS (Figure 6). Internal tides and ISWs are observed to the south and north of the conversion source, respectively

21699291, 2020, 11, Downloaded from https://agupubs.onlinelibrary.wiley.com/doi/10.1029/2020JC016554 by University Of Washington, Wiley Online Library on [15/09/2025]. See the Terms and Conditions (https://onlinelibrary.wiley.com/terms-and-conditions) on Wiley Online Library for rules of use; OA articles are governed by the applicable Creative Commons License

21699291, 2020, 11, Downloaded from https://agupubs.onlinelibrary.wiley.com/doi/10.1029/2020JC016554 by University Of Washington, Wiley Online Library on [15/09/2025]. See the Terms and Conditions (https://onlinelibrary.wiley.com/terms-and-conditions) on Wiley Online Library for rules of use; OA articles are governed by the applicable Creative Commons License

(Figure 10). It is suggested that the onshore radiation evolves into ISWs in shallow water and the offshore radiation propagates as linear internal tides in deep water. Based on the 26-year-long coherent results, the lower-bound southward M_2 energy flux is 0.18 GW, about 10% of the westward energy flux from the Luzon Strait.

The four major tidal constituents (M_2, S_2, K_1, and O_1) have been studied using the same data set and by the same mapping technique. The results show that the continental slope radiates southward semidiurnal M_2 and S_2 internal tides (Figure 12), but no diurnal K_1 and O_1 internal tides are observed (Figure 13).

Previous studies have shown that the internal tide field subjects to strong temporal variations due to Kuroshio intrusion, seasonal stratification, and mesoscale eddies. This study shows that multiwave interference also causes spatial variability in internal tide properties (Figure 11). This study cautions the simple attribution of internal tide variations to the Kuroshio intrusion and/or mesoscale eddies. It is difficult to distinguish the variations caused by ocean dynamic processes and by multiwave interference. A proper approach is separately resolving internal tides of different propagation directions using the method presented in this paper. Then, the temporal variations can be studied following individual long-range internal tidal beams.

Data Availability Statement

The barotropic tide model TPXO8 was constructed and made freely available (http://volkov.oce.orst.edu/tides/tpxo8_atlas.html) by Prof. G. Egbert and Dr. S. Erofeeva (Oregon State University). The World Ocean Atlas 2013 is produced and made available by NOAA National Oceanographic Data Center (https://www.nodc.noaa.gov/OC5/woa13/). The internal tide models developed in this study have been published and made available to the oceanographic community (https://doi.org/10.6084/m9.figshare.12811586). Contact the author for further instructions (zzhao@apl.uw.edu).

Acknowledgments
This work was partly supported by the National Aeronautics and Space Administration (NASA) via projects NNX17AH57G and 80NSSC18K0771, and the National Science Foundation (NSF) via project OCE1634041. The author thanks Dr. Xiaolin Bai (Xiamen University) for providing the geographic distribution of internal solitary waves observed by MODIS true-color images. The author thanks Drs. Xiaolin Bai, Zhiyu Liu, and Quanan Zheng for helpful discussions. The author thanks three anonymous reviewers for their constructive suggestions that greatly improved the quality of this paper. The satellite altimeter products were produced by Ssalto/Duacs and distributed by AVISO (Archiving, Validation, and Interpretation of Satellite Oceanographic Data) with support from CNES (http://www.aviso.altimetry.fr) and the Copernicus Marine Environment Monitoring Service (http://marine.copernicus.eu).

References

Alford, M. H., Peacock, T., MacKinnon, J. A., Nash, J. D., Buijsman, M. C., Centurioni, L. R., et al. (2015). The formation and fate of internal waves in the South China Sea. *Nature*, *521*, 65–69. https://doi.org/10.1038/nature14399

Bai, X., Liu, Z., Li, X., & Hu, J. (2014). Generation sites of internal solitary waves in the southern Taiwan Strait revealed by MODIS true-colour image observations. *International Journal of Remote Sensing*, *35*(11–12), 4086–4098. https://doi.org/10.1080/01431161.2014.916453

Bai, X., Liu, Z., Zheng, Q., Hu, J., Lamb, K. G., & Cai, S. (2019). Fission of shoaling internal waves on the northeastern shelf of the South China Sea. *Journal of Geophysical Research: Oceans*, *124*, 4529–4545. https://doi.org/10.1029/2018JC014437

Buijsman, M. C., Kanarska, Y., & McWilliams, J. C. (2010). On the generation and evolution of nonlinear internal waves in the South China Sea. *Journal of Geophysical Research*, *115*, C02012. https://doi.org/10.1029/2009JC005275

Chiou, M. D., Jan, S., Wang, J., Lien, R. C., & Chien, H. (2011). Source of baroclinic tidal energy in the Gaoping Submarine Canyon off southwestern Taiwan. *Journal of Geophysical Research*, *116*, C12016. https://doi.org/10.1029/2011JC007366

Egbert, G. D., & Erofeeva, S. Y. (2002). Efficient inverse modeling of barotropic ocean tides. *Journal of Atmospheric and Oceanic Technology*, *19*, 183–204.

Fett, R., & Rabe, K. (1977). Satellite observation of internal wave refraction in the South China Sea. *Geophysical Research Letters*, *4*, 189–191. https://doi.org/10.1029/GL004i005p00189

Gill, A. E. (1982). *Atmosphere-ocean dynamics*. Cambridge, MA: Academic Press.

Huang, X., Wang, Z., Zhang, Z., Yang, Y., Zhou, C., Yang, Q., & Tian, J. (2018). Role of mesoscale eddies in modulating the semidiurnal internal tide: Observation results in the northern South China Sea. *Journal of Physical Oceanography*, *48*(8), 1749–1770. https://doi.org/10.1175/JPO-D-17-0209.1

Jackson, C. R. (2009). An empirical model for estimating the geographic location of nonlinear internal solitary waves. *Journal of Atmospheric and Oceanic Technology*, *26*, 2243–2255. https://doi.org/10.1175/2009JTECHO638.1

Jan, S., Lien, R. C., & Ting, C. H. (2008). Numerical study of baroclinic tides in Luzon Strait. *Journal of Oceanography*, *64*(5), 789–802.

Johnston, T. M. S., Rudnick, D. L., & Kelly, S. M. (2015). Standing internal tides in the Tasman Sea observed by gliders. *Journal of Physical Oceanography*, *45*, 2715–2737. https://doi.org/10.1175/JPO-D-15-0038.1

Kelly, S. M. (2016). The vertical mode decomposition of surface and internal tides in the presence of a free surface and arbitrary topography. *Journal of Physical Oceanography*, *46*(12), 377–3788. https://doi.org/10.1175/JPO-D-16-0131.1

Kerry, C. G., Powell, B. S., & Carter, G. S. (2013). Effects of remote generation sites on model estimates of M_2 internal tides in the Philippine Sea. *Journal of Physical Oceanography*, *43*(1), 187–204. https://doi.org/10.1175/JPO-D-12-081.1

Klymak, J. M., Alford, M. H., Pinkel, R., Lien, R. C., Yang, Y. J., & Tang, T. Y. (2011). The breaking and scattering of the internal tide on a continental slope. *Journal of Physical Oceanography*, *41*(5), 926–945. https://doi.org/10.1175/2010JPO4500.1

Lai, Z., Jin, G., Huang, Y., Chen, H., Shang, X., & Xiong, X. (2019). The generation of nonlinear internal waves in the South China Sea: A three-dimensional, nonhydrostatic numerical study. *Journal of Geophysical Research: Oceans*, *124*, 8949–8968. https://doi.org/10.1029/2019JC015283

Li, Q., Wang, B., Chen, X., Chen, X., & Park, J. H. (2016). Variability of nonlinear internal waves in the South China Sea affected by the Kuroshio and mesoscale eddies. *Journal of Geophysical Research: Oceans*, *121*, 2098–2118. https://doi.org/10.1002/2015JC011134

Liu, A. K., Chang, Y. S., Hsu, M. K., & Liang, N. K. (1998). Evolution of nonlinear internal waves in the East and South China Sea. *Journal of Geophysical Research*, *103*(C4), 7995–8008.

Locarnini, R. A., Mishonov, A. V., Antonov, J. I., Boyer, T. P., Garcia, H. E., Baranova, O. K., & Seidov, D. (2013). World Ocean Atlas 2013, Volume 1: Temperature NOAA Atlas NESDIS 73. https://data.nodc.noaa.gov/woa/WOA13/DOC/woa13_vol1.pdf

Martini, K. I., Alford, M. H., Nash, J. D., Kunze, E., & Merrifield, M. A. (2007). Diagnosing a partly-standing internal wave in Mamala Bay, Oahu. *Geophysical Research Letters*, *34*, L17604. https://doi.org/10.1029/2007GL029749

Min, W., Li, Q., Zhang, P., Xu, Z., & Yin, B. (2019). Generation and evolution of internal solitary waves in the southern Taiwan Strait. *Geophysical and Astrophysical Fluid Dynamics*, *113*(3), 287–302. https://doi.org/10.1080/03091929.2019.1590568

Nash, J. D., Kunze, E., Lee, C. M., & Sanford, T. B. (2006). Structure of the baroclinic tide generated at Kaena Ridge, Hawaii. *Journal of Physical Oceanography*, *36*, 1123–1135.

Niwa, Y., & Hibiya, T. (2004). Three-dimensional numerical simulation of M_2 internal tides in the East China Sea. *Journal of Geophysical Research*, *109*, C04027. https://doi.org/10.1029/2003JC001923

Park, J. H., & Farmer, D. (2013). Effects of Kuroshio intrusions on nonlinear internal waves in the South China Sea during winter. *Journal of Geophysical Research: Oceans*, *118*, 7081–7094. https://doi.org/10.1002/2013JC008983

Rainville, L., Johnston, T. M. S., Carter, G. S., Merrifield, M. A., Pinkel, R., Worcester, P. F., & Dushaw, B. D. (2010). Interference pattern and propagation of the M2 internal tide south of the Hawaiian Ridge. *Journal of Physical Oceanography*, *40*, 311–325. https://doi.org/10.1175/2009JPO4256.1

Ray, R. D., & Zaron, E. D. (2011). Non-stationary internal tides observed with satellite altimetry. *Geophysical Research Letters*, *38*, L17609. https://doi.org/10.1029/2011GL048617

Ray, R. D., & Zaron, E. (2016). M_2 internal tides and their observed wavenumber spectra from satellite altimetry. *Journal of Physical Oceanography*, *46*(1), 3–22. https://doi.org/10.1175/JPO-D-15-0065.1

Simmons, H., Chang, M. H., Chang, Y. T., Chao, S. Y., Fringer, O., Jackson, C. R., & Ko, D. S. (2011). Modeling and prediction of internal waves in the South China Sea. *Oceanography*, *24*(4), 88–99. https://doi.org/10.5670/oceanog.2011.97

Smith, W. H. F., & Sandwell, D. T. (1997). Global sea floor topography from satellite altimetry and ship depth soundings. *Science*, *277*, 1956–1962.

Vlasenko, V., Stashchuk, N., Guo, C., & Chen, X. (2010). Multimodal structure of baroclinic tides in the South China Sea. *Nonlinear Processes in Geophysics*, *17*, 529–543. https://doi.org/10.5194/npg-17-529-2010

Wang, J., Huang, W., Yang, J., Zhang, H., & Zheng, G. (2012). Study of the propagation direction of the internal waves in the South China Sea using satellite images. *Acta Oceanologica Sinica*, *32*(5), 42–50. https://doi.org/10.1007/s13131-013-0312-6

Wang, X., Peng, S., Liu, Z., Huang, R. X., Qian, Y. K., & Li, Y. (2016). Tidal mixing in the South China Sea: An estimate based on the internal tide energetics. *Journal of Physical Oceanography*, *46*(1), 107–124. https://doi.org/10.1175/JPO-D-15-0082.1

Wang, Y., Xu, Z., Yin, B., Hou, Y., & Chang, H. (2018). Long-ange radiation and interference pattern of multisource M_2 internal tides in the Philippine Sea. *Journal of Geophysical Research: Oceans*, *123*, 5091–5112. https://doi.org/10.1029/2018JC013910

Wingham, D. J., Francis, C. R., Baker, S., Bouzinac, C., Cullen, R., de Chateau-Thierry, P., & Wallis, D. (2006). CryoSat: A mission to determine the fluctuations in Earth's land and marine ice fields. *Advances in Space Research*, *37*, 841–871.

Xu, Z., Liu, K., Yin, B., Zhao, Z., Wang, Y., & Li, Q. (2016). Long-range propagation and associated variability of internal tides in the South China Sea. *Journal of Geophysical Research: Oceans*, *121*, 8268–8286. https://doi.org/10.1002/2016JC012105

Yu, H., Yu, H., Wang, L., Kuang, L., Wang, H., Ding, Y., & Lawen, J. (2017). Tidal propagation and dissipation in the Taiwan Strait. *Continental Shelf Research*, *136*, 57–73. https://doi.org/10.1016/j.csr.2016.12.006

Zaron, E. D. (2015). Nonstationary internal tides observed using dual-satellite altimetry. *Journal of Physical Oceanography*, *45*, 2239–2246. https://doi.org/10.1175/JPO-D-15-0020.1

Zaron, E. D. (2017). Mapping the nonstationary internal tide with satellite altimetry. *Journal of Geophysical Research: Oceans*, *122*, 539–554. https://doi.org/10.1002/2016JC012487

Zaron, E. D. (2019). Baroclinic tidal sea level from exact-repeating mission altimetry. *Journal of Physical Oceanography*, *49*, 193–210. https://doi.org/10.1175/JPO-D-18-0127.1

Zhai, R. W., Chen, G. Y., Liang, C. R., Shang, X. D., & Xie, J. S. (2020). The influence of ENSO on the structure of internal tides in the Xisha area. *Journal of Geophysical Research: Oceans*, *125*, e2019JC015405. https://doi.org/10.1029/2019JC015405

Zhang, Z., Fringer, O. B., & Ramp, S. R. (2011). Three-dimensional, nonhydrostatic numerical simulation of nonlinear internal wave generation and propagation in the South China Sea. *Journal of Geophysical Research*, *116*, C05022. https://doi.org/10.1029/2010JC006424

Zhao, Z. (2014). Internal tide radiation from the Luzon Strait. *Journal of Geophysical Research: Oceans*, *119*, 5434–5448. https://doi.org/10.1024/2014JC010014

Zhao, Z. (2016). Using CryoSat-2 altimeter data to evaluate M_2 internal tides observed from multisatellite altimetry. *Journal of Geophysical Research: Oceans*, *121*, 5164–5180. https://doi.org/10.1029/2016JC011805

Zhao, Z. (2019). Mapping internal tides from satellite altimetry without blind directions. *Journal of Geophysical Research: Oceans*, *124*, 8605–8625. https://doi.org/10.1029/2019JC015507

Zhao, Z., Alford, M. H., Girton, J. B., Rainville, L., & Simmons, H. L. (2016). Global observations of open-ocean mode-1 M_2 internal tides. *Journal of Physical Oceanography*, *46*, 1657–1684. https://doi.org/10.1175/JPO-D-15-0105.1

Zhao, Z., Alford, M. H., MacKinnon, J. A., & Pinkel, R. (2010). Long-range propagation of the semidiurnal internal tide from the Hawaiian Ridge. *Journal of Physical Oceanography*, *40*, 713–736. https://doi.org/10.1175/2009JPO4207.1

Zhao, Z., Klemas, V., Zheng, Q., & Yan, X. H. (2004). Remote sensing evidence for baroclinic tide origin of internal solitary waves in the northeastern South China Sea. *Geophysical Research Letters*, *31*, L06302. https://doi.org/10.1029/2003GL019077

Zheng, Q., Susanto, R. D., Ho, C. R., Song, Y. T., & Xu, Q. (2007). Statistcal and dynamical analyses of generation mechanism of solitary internal waves in the northern South China Sea. *Journal of Geophysical Research*, *112*, C03021. https://doi.org/10.1029/2006JC003551

Zu, T., Gan, J., & Erofeeva, S. Y. (2008). Numerical study of the tide and tidal dynamics in the South China Sea. *Deep Sea Research Part I: Oceanographic Research Papers*, *55*(2), 137–154. https://doi.org/10.1016/j.dsr.2007.10.007

Zweng, M., Reagan, J., Antonov, J., Locarnini, R., Mishonov, A., Boyer, T., & Biddle, M. (2013). World Ocean Atlas 2013, Volume 2: Salinity. NOAA Atlas NESDIS 74. Retrieved from https://data.nodc.noaa.gov/woa/WOA13/DOC/woa13_vol2.pdf

21699291, 2020, 11, Downloaded from https://agupubs.onlinelibrary.wiley.com/doi/10.1029/2020JC016554 by University Of Washington, Wiley Online Library on [15/09/2025]. See the Terms and Conditions (https://onlinelibrary.wiley.com/terms-and-conditions) on Wiley Online Library for rules of use; OA articles are governed by the applicable Creative Commons License